Energy Materials and Devices

Research Article

# Bulk nanoporous platinum for electrochemical actuation

Haonan Sun, Yizhou Huang, and Shan Shi ✉

## Graphical Abstract

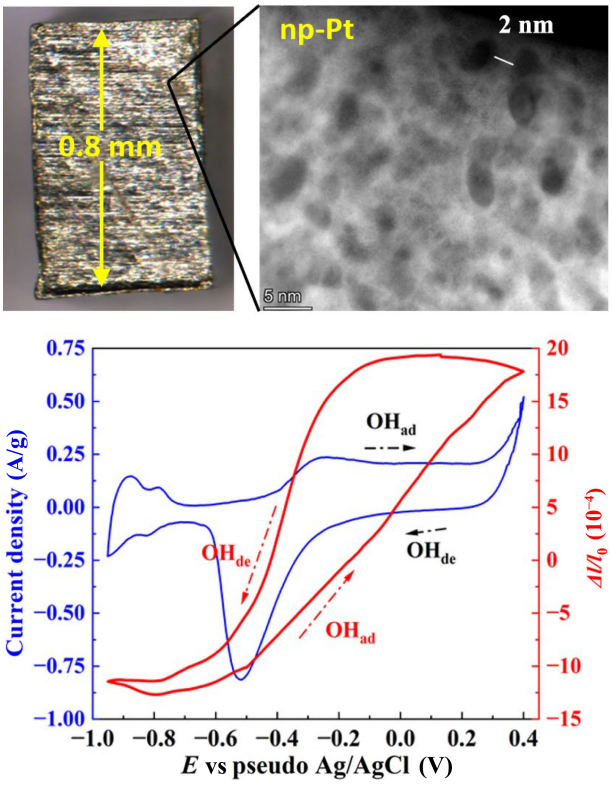


Bulk nanoporous platinum with ultrafine structure size (ligament size: 2 nm) has been prepared for the first time by electrochemical dealloying of $Cu_{85}Pt_{15}$ in $H_2SO_4$ at 60 ℃. This material exhibits a large electrochemically active surface area (25 $m^2/g$) , and excellent actuation performance (working voltage: 1 V; strain amplitude: 0.37%: strain energy density: 1.64 $MJ/m^3$) .

✉Address correspondence to Shan Shi, shan.shi@tuhh.de, https://www.tuhh.de/wp/mitarbeit-ende/professor/innen/shan-shi

**Received:** August 27, 2023
**Revised:** September 25, 2023
**Accepted:** September 26, 2023

https://www.sciopen.com/journal/3005-3315

https://mc03.manuscriptcentral.com/emd

**Citation:** Sun H., Huang Y., Shi S. Bulk nanoporous platinum for electrochemical actuation. *Energy Mater. Devices*, 2023, 1, 9370006. https://doi.org/10.26599/EMD.2023.9370006

Energy Materials and Devices

Research Article https://doi.org/10.26599/EMD.2023.9370006

# Bulk nanoporous platinum for electrochemical actuation

Haonan Sun[1], Yizhou Huang[1], and Shan Shi[1,2] ✉

[1] *Research Group of Integrated Metallic Nanomaterials Systems, Hamburg University of Technology, Hamburg, Germany*
[2] *Institute of Materials Mechanics, Helmholtz-Zentrum Hereon, Geesthacht, Germany*

**Received:** August 27, 2023 / **Revised:** September 25, 2023 / **Accepted:** September 26, 2023

## ABSTRACT

Bulk nanoporous platinum (np-Pt) samples with a remarkably fine ligament size down to 2 nm and good mechanical robustness were fabricated for the first time by electrochemically dealloying $Pt_{15}Cu_{85}$ master alloy in 1 mol $L^{-1}$ $H_2SO_4$ at 60 ℃. The as-prepared np-Pt shows an electrochemically active specific surface area as high as 25 $m^2/g$ due to the ultrafine nanostructure. The active surface area remains almost invariable even after 15% macroscopic compressive strain. Furthermore, np-Pt shows considerably high thermal stability due to the low surface diffusivity of Pt. Np-Pt is a promising surface- or interface-controlled functional material, particularly when excellent electrochemical and mechanical performance are necessary due to its high surface-to-volume ratio and mechanical robustness. This work demonstrated the potential application of np-Pt as an electrochemical actuation material. In-situ dilatometry experiments revealed that the surface adsorption–desorption of OH species on np-Pt causes significant strain variations. The proposed np-Pt electrochemical actuator shows an operating voltage down to 1.0 V, a large reversible strain amplitude of 0.37%, and a strain energy density of 1.64 $MJ/m^3$.

## KEYWORDS

nanoporous platinum, dealloying, actuators, electrochemical active surface area

## 1 Introduction

Nanoporous materials, renowned for their intricate pore networks and large specific surface areas, are capturing attention across diverse fields for their distinctive attributes and versatile applications such as energy storage, catalysis, sensors, and optical and photonic devices[1-9]. Nanoporous metals are gaining particular interest with their good electrochemical and mechanical performances, showing considerable potential as actuation materials[10, 11]. The evolving landscape of actuation has undergone a significant shift with the emergence of materials capable of reversible dimensional alterations triggered by external stimuli, such as applied voltage. Piezoelectric ceramics and conducting polymers have been intensively investigated as actuation materials[12-16], while the realm of low-voltage-induced actuation in metals remains an intriguing and relatively underexplored domain. The search for high-performance actuators demands a delicate balance between large actuation strokes and robust strength, which is crucial for achieving heightened work density. Piezoelectric ceramic actuators typically exhibit impressive stiffness and strength, but their strain amplitude remains constrained within 0.1%–0.2%[17, 18]. Conversely, polymer actuators explore the other end of the spectrum, boasting exceptionally large reversible strains (>100%), which are often similar to artificial muscles[15, 18]. However, their mechanical performance is compromised by low stiffness and strength. Therefore, sustainable and bulk nanoporous metals made by dealloying have emerged as an attractive type of actuation material in the past two decades. Bulk nanoporous metal-based actuators demonstrate substantially lower initial driving voltages and greater strain amplitudes than commercial piezo actuators while revealing good mechanical properties[19, 20].

The functionality of nanoporous metals as actuators hinges on the exploitation of surface stress varia-

✉ Address correspondence to Shan Shi, shan.shi@tuhh.de

tion, orchestrating significant compensatory stress and strain within their solid skeleton[21]. These phenomena have been observed in various nanoporous metals, notably Pt[11, 22], Pd[23, 24], and Au[25, 26]. Moreover, reducing the ligament size in these metals, which is defined as the diameter of the ligament, can not only increase their surface-to-volume ratio or specific surface area but also enhance their mechanical properties[27]. Consequently, this augmentation facilitates the realization of additional substantial actuation strains and work density. Thus, the avenue for elevating actuation performance in nanoporous materials emerges through the deliberate reduction of their structure size. For instance, Jin et al. found that the actuation amplitude is substantially enhanced when decreasing the ligament size of dealloying-made nanoporous gold down to 5 nm[28]. Dealloying involves the selective dissolution of less noble components and the reorganization of remaining noble metals to form a bicontinuous nanoporous structure[29-31]. This method has already been used to synthesize millimeter- or centimeter-sized nanoporous Au and Pd[10, 23, 25, 26].

This work fabricates uniform and ultrafine nanoporous Pt (np-Pt) in a macroscopic body for the first time. The millimeter-sized np-Pt was successfully synthesized via electrochemically dealloying $Pt_{15}Cu_{85}$ master alloy in 1 mol $L^{-1}$ $H_2SO_4$ aqueous solution at 60 ℃. The resulting microstructure reveals a refined nanostructure with the ligament size down to 2 nm, a uniform distribution of residual Cu in np-Pt, and a large electrochemically active surface area reaching up to 25 $m^2/g$ at a compressive strain of 0%–15%. The in-situ dilatometry experiments reveal extraordinary actuation performance: an operating voltage down to 1.0 V, a linear strain amplitude up to 0.37%, and a work density of 1.64 $MJ/m^3$.

## 2 Experimental

$Pt_{15}Cu_{85}$ master alloy was produced by alloying Cu wires (99.99%, Alfa Aesar) and Pt wires (99.95%, Heraeus Metals) through repeated melting–solidification in an arc melter (MAM-1 Edmund Bühler). Subsequently, the alloys underwent annealing at 1000 ℃ for over seven days and were rapidly quenched in water. The ingot was then cold-rolled by using a manual rolling mill to 1 mm thickness and then cut into 0.65 mm × 0.8 mm × 1 mm cuboids. Nanoporous Pt was generated through dealloying in a 1 mol $L^{-1}$ $H_2SO_4$ aqueous solution (Suprapur, Merck), thereby utilizing a three-electrode cell setup. A Ag/AgCl pseudo-reference electrode was made based on ref. [26] and was used throughout this study. A carbon fiber cloth (with a specific surface area of 1200–1750 $m^2/g$, Kynol) was used as the counter electrode. A refrigerated circulator was then utilized to maintain the electrolyte temperature at 60 ℃ during dealloying processes.

The dealloying was conducted by applying a constant electrode potential at 0.22 and 0.40 V until the current decays to 10 and 2 μA, respectively. The low dealloying potential value of 0.22 V is used to provide a decent dealloying speed and avoid cracks induced by rapid dealloying. A subsequent high potential value of 0.40 V is used to further reduce the residual Cu content. Following the completion of the procedure, cyclic voltammetry (CV) cycles were executed, spanning from −0.20 to 0.80 V, and repeated 20 times at a scan rate of 10 mV/s to further reduce residual Cu. A potentiostat (PGSTAT302N, Metrohm) was used to control the potential accurately. After the dealloying processes, the samples were then immersed in deionized water (Ultra Clear TWF UV TM, Siemens) for a minimum of 12 h, followed by a subsequent immersion in ethanol (≥ 99.5%) for at least 6 h before undergoing drying in an argon atmosphere.

The phase information of np-Pt was characterized using an X-ray diffractometer (Bruker D8 Advance) with a Cu Kα radiation source. Scanning electron microscopes (SEM, FEI Helios Nano Lab G3) equipped with an immersion lens were utilized for the microstructure analysis. Cross-sectional surfaces through the center of the sample were achieved through precision cutting using a scalpel, leading to a cleaved section to gain insight into the internal structure. The composition of these cross-sections was then analyzed using energy-dispersive X-ray analysis. Transmission electron microscopy (TEM) images were acquired by utilizing the Cs-corrected transmission electron microscope Titan Cubed Themis G2 300 operated at an accelerating voltage of 300 kV to examine the microstructure at a fine scale. The TEM specimen was prepared by ultrasonic treatment of the sample in water, followed by deposition onto a molybdenum (Mo) grid through drop-casting.

The testing machine (Zwick 1474), equipped with an in situ digital image correlation (DIC) system (DaVis 8.2.0, LaVision), an electrochemical cell, and a potentiostat, was used for measuring the surface area at different compressive strains. An engineering strain rate of $10^{-4}$/s was maintained throughout the tests, commencing with a preload of 0.5 N at the outset of each measurement. The length variation of the sample with electrode potential at room temperature was monitored using an in-situ dilatometer (Linseis L75V) setup, as described in refs. [23, 24]. 1 mol $L^{-1}$ $H_2SO_4$ (Suprapur, Merck) and 1 mol $L^{-1}$ KOH (≥99.5%, Merck) were used during the actuation test. The Ag/AgCl pseudo-reference electrode and Pt plate (99.95%, Heraeus Metals) were used as reference and counter electrodes, respectively.

## 3 Results and discussion

### 3.1 Microstructure and phase

The macrostructure and microstructure of the np-Pt were investigated using an optical microscope and SEM, respectively. Figure 1a shows the $Pt_{15}Cu_{85}$ master alloy (left) and the np-Pt after dealloying (right). The master alloy possesses dimensions of 1.0 mm × 0.65 mm × 0.8 mm, while the np-Pt sample measures approximately 0.78 mm × 0.56 mm × 0.64 mm. Notably, despite experiencing a ~50% volume shrinkage, the np-Pt remains a macroscopic bulk throughout the entire manufacturing process. Figure 1b shows the X-ray diffraction result of as-prepared np-Pt perpendicular to the rolling direction. The diffraction pattern of the np-Pt sample displays peaks at $2\theta$ = 40°, 47°, 69°, 83°, and 87° corresponding to the reflection from (1 1 1), (2 0 0), (2 2 0), (3 1 1), and (2 2 2) planes of the face-centered cubic (fcc) crystal structure, respectively. This observation indicates the acquisition of a single fcc Pt-Cu phase after dealloying. The bicontinuous nanoporous structure of np-Pt is visible in its SEM image shown in Fig. 1c. However, the precise determination of its ligament size is beyond the resolution limit of this SEM image. np-Pt is annealed at 300 ℃ for 20 min in a vacuum to confirm its good thermal stability. Figure 1d depicts that the ligament size of coarsened np-Pt is as low as 6 nm, indicating its high thermal stability.

Figures 2a and 2b show the TEM images of the as-prepared np-Pt. The figure indicates that the ligament size of as-prepared np-Pt is extremely small, approximately 2 nm. In addition, scanning transmission electron microscopy and energy-dispersive X-ray spectroscopy (STEM–EDS) analysis in Figs. 2d–2f detected a homogeneous chemical distribution in np-Pt. The uniform element distribution (8 ± 2 at% O, 22 ± 3 at% Cu, 70 ± 3 at% Pt) is observed across the entire sample, indicating complete dealloying and a uniform porosity throughout the specimen.

### 3.2 Electrochemically active surface area

The hydrogen desorption charge integration method is employed to determine the electrochemical active surface area (ECSA) of as-prepared np-Pt bulk samples[32, 33] and estimate the ECSA by using the following formula[34]:

$$\mathrm{ECSA} = Q_{\mathrm{H}}/(m \times 210\ \mu\mathrm{C/cm^2}) \quad (1)$$

where $m$ is the mass of np-Pt, and $Q_{\mathrm{H}}$ is the integrated charge associated with the hydrogen electrosorption peaks obtained from CV measurements. The unit specific charge density, 210 μC/cm², is associated with the electrosorption of one monolayer of hydrogen on a planar Pt electrode[35].

The ECSAs of np-Pt were measured at different engineering strains ($\varepsilon_{\mathrm{eng}}$) to assess the influence of mechanical load on the electrochemically active surface area of np-Pt. The CV measurements were conducted within a potential range between −0.60 and 0.75 V (vs. Ag/AgCl pseudo-reference electrode) at 100 mV/s in 1 mol $L^{-1}$ $H_2SO_4$ until a steady-state

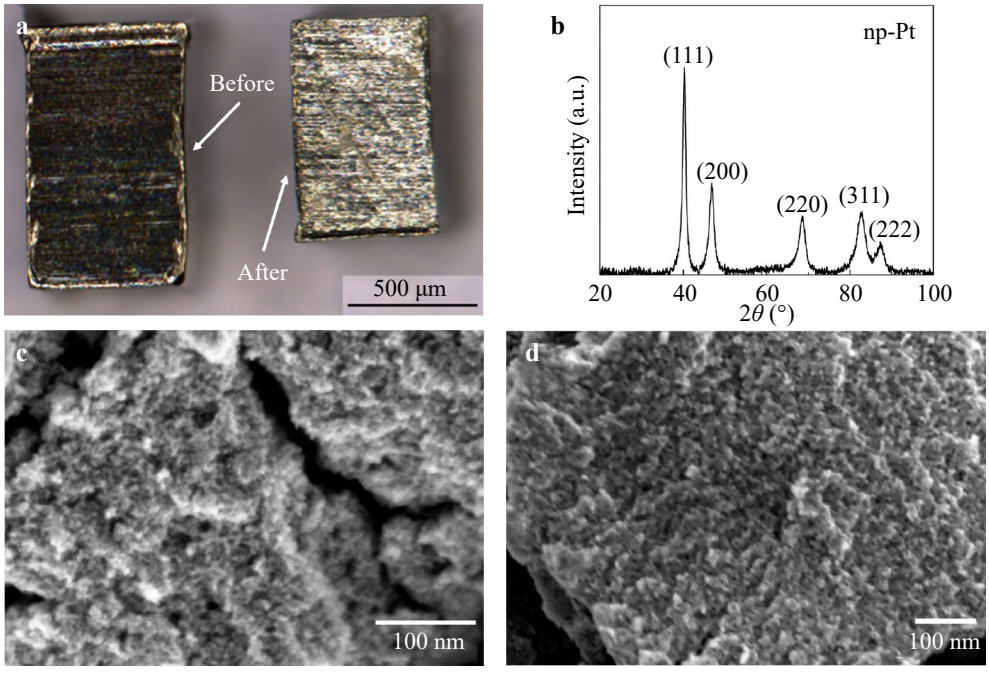


**Figure 1** (a) Optical microscope photos of $Pd_{15}Cu_{85}$ master alloy (left, before dealloying) and np-Pt (right, after dealloying). (b) X-ray diffraction pattern of np-Pt perpendicular to the rolling direction. (c) SEM image of np-Pt. (d) SEM image of np-Pt after thermal treatment at 300 ℃ for 20 min in a vacuum.

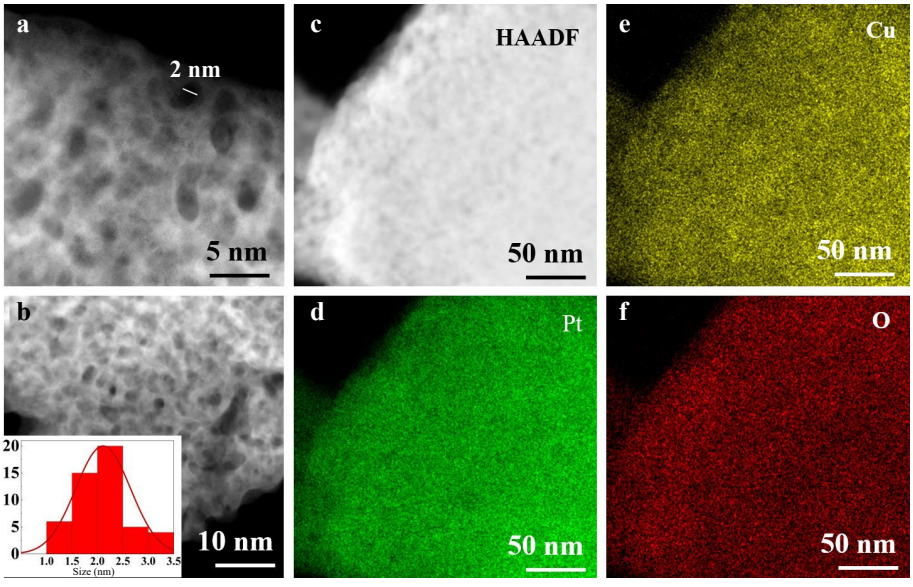


**Figure 2** (a) TEM images of np-Pt. (b) TEM images of np-Pt and an insert chart showing the statistics on the distribution of ligament sizes. (c–f) High-angle annular dark field (HAADF) STEM–EDS images of np-Pt. Note the ultrafine ligament size of 2 nm marked in (a) and the uniform composition indicated in (d–f).

voltammogram was attained, offering an insightful estimation of the ECSA. Figure 3a illustrates the cyclic voltammograms of the np-Pt at $\varepsilon_{eng}$ of 0%, 7.5%, and 15%. The desorption peaks exhibit minimal variation, signifying the stability of the surface area during deformation. Figure 3b shows the corresponding ECSAs (25.6, 25.3, and 24.7 $m^2/g$) and flow stress ($\sigma_{eng}$ = 0, 10, and 27 MPa) at $\varepsilon_{eng}$ = 0%, 7.5%, and 15%, respectively. Figure 3c shows the schematic of strain tests on mm-sized np-Pt with a high-speed camera. Figures 3d and 3e reveal the photographs of the np-Pt before and after 15% compressive deformation in electrolytes. The strain measurements from the mechanical tests underwent rigorous analysis using DIC to ensure the accurate calculation of sample deformation. Figures 3f and 3g show the deformation intensity maps at $\varepsilon_{eng}$ = 0% and $\varepsilon_{eng}$ = 15%, respectively, captured during the DIC process.

The features, including the large electrochemically active surface area and the almost 100% surface area retention under high deformation, provide substantial potential for bulk ultrafine np-Pt in various applications that require excellent electrochemical and mechanical performances, such as lightweight functional, actuation, and strain sensing materials.

### 3.3 Actuation performance

Substantial amplification in deformations emerged as the potential spanned a broad array of voltages, encompassing domains of specific adsorption. The actuation performances of np-Pt were measured in two distinct electrolytes, namely 1 mol $L^{-1}$ $H_2SO_4$ and 1 mol $L^{-1}$ KOH, using an in-situ dilatometer setup.

Figure 4a illustrates the CV curves of np-Pt in 1 mol $L^{-1}$ $H_2SO_4$ within different potential windows. The upper vertex potential was held constant at 0.7 V, while the lower vertex potential underwent a sequential reduction. Starting at −0.5 V, the lower vertex potential was subsequently reduced by 0.1 V following every 10 cycles, originating from 0.3 V and employing a scan rate of 10 mV/s. The redox peaks corresponding to the adsorption–desorption of OH species (shortly, $OH_{ad}$ and $OH_{de}$) at the positive potential regime are displayed and marked in Fig. 4a. The schematic of the experimental setup, the in-situ dilatometer, for the actuation test is presented in Fig. 4b.

Figure 4c shows the relative length variation recorded simultaneously during the potential sweeps. The figure reveals that the maximum strain amplitude at a fixed scan rate can be easily controlled by adjusting the potential window. The maximum strain amplitude of np-Pt in 1 mol $L^{-1}$ $H_2SO_4$ reaches up to 0.04%. However, a linear, irreversible shrinkage of approximately 0.1% appeared in np-Pt after nearly 100 cycles. This kind of shrinkage has also been reported in other np metal actuators[11, 23, 28].

As a function of potential, Fig. 4d shows the reversible cyclic length variation within a wide potential window of 0–0.7 V is plotted together with current density variation to understand the actuation mechanism. This finding indicates that the 0.04% reversible linear strain is caused by OH adsorption–desorption-induced surface stress variation. This phenomenon agrees well with literature reports on pure Pt[11, 22, 36]. The actuation is caused by the variation of surface stress with electrode potential. The surface stress induced by the surface OH adsorbates must be compensated by the bulk stress, leading to a macroscopic elastic strain. Different

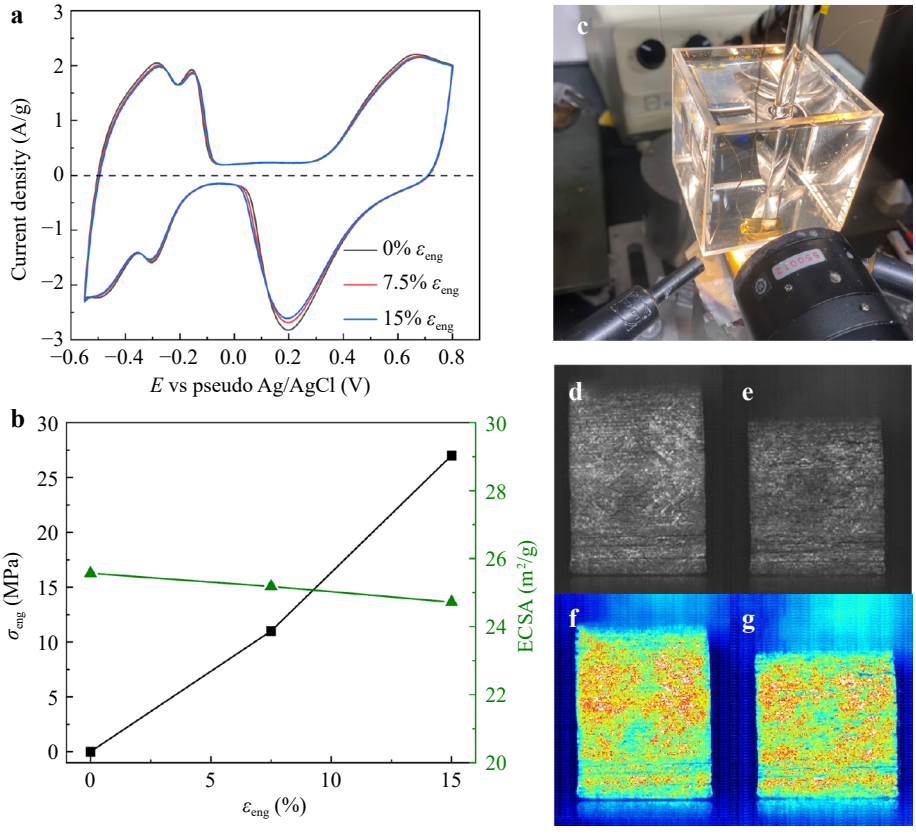


**Figure 3** (a) Cyclic voltammogram for np-Pt in 1 mol $L^{-1}$ $H_2SO_4$ at an engineering strain ($\varepsilon_{eng}$) of 0%, 7.5%, and 15%. (b) Flow stress ($\sigma_{eng}$) and ECSAs as a function of $\varepsilon_{eng}$. (c) Schematic of a mechanical testing device equipped with an electrochemical cell and a high-speed camera. One mm-sized np-Pt is placed in a chemical cell and compressed by the quartz pushrod of the testing device. Photographs of np-Pt at (d) $\varepsilon_{eng}$ = 0, and (e) $\varepsilon_{eng}$ =15%. Deformation intensity maps captured during the DIC process for the sample at (f) $\varepsilon_{eng}$ = 0% and (g) $\varepsilon_{eng}$ = 15%.

from literature reports on pure Pt, except for the increasing dominant length with rising electrode potential, Fig. 4d shows that the length of the proposed np-Pt decreases with increasing potential in the middle regime of the potential window. This phenomenon might be caused by Cu dissolution during a positive potential scan and redeposition during a negative potential scan in acids [37].

Electrochemical actuation measurements were also conducted in 1 mol $L^{-1}$ KOH solutions on a nominally identical sample at different scan rates. Fig. 5a shows the CV curves of np-Pt in KOH at scan rates ranging from 1 to 0.2 mV/s. The H and OH adsorption–desorption peaks are presented in all these CV curves.

Figure 5b shows the reversible relative length variation measured simultaneously with CV. Remarkably, the overall reversible strain amplitude of np-Pt in 1 mol $L^{-1}$ KOH is up to 0.37%, which has a value that is 2.5 times larger than that of a Pt (crystalline size: 6 nm) actuator in the same electrolyte 0.15%[11]. This finding is attributed to the substantially small ligament size and large electrochemically active surface area of the dealloying-made np-Pt in this work.

Moreover, the influence of scan rate on the strain amplitude is investigated. The relative length change $\Delta l/l_0$ during cyclic potential sweep at different scan rates of 1, 0.8, 0.4, and 0.2 mV/s is displayed in Fig. 5c. The results reveal that the overall actuation amplitude is independent of the scan rate, implying that OH adsorption–desorption processes are not limited by the diffusion kinetics in ultrafine pore space in the investigated scan rate regime.

In addition to linear actuation amplitude and response time, the actuation performances including volumetric work density ($W_V$) and mass-specific strain energy density ($W_M$) are also evaluated on np-Pt actuators. This approach is of particular interest when bulk np metal actuators are used in devices capitalizing on the volume change of porous metal to perform work against external pressure.

The estimation of $W_V$ and $W_M$ used the following two formulas[38]:

$$W_V = 1/2 Y_{eff} \varepsilon_{max}^2 \quad (2)$$

$$W_M = W_V/\rho \quad (3)$$

where $\varepsilon_{max}$ denotes the maximum relative volume change, $\rho$ denotes the density of the porous material,

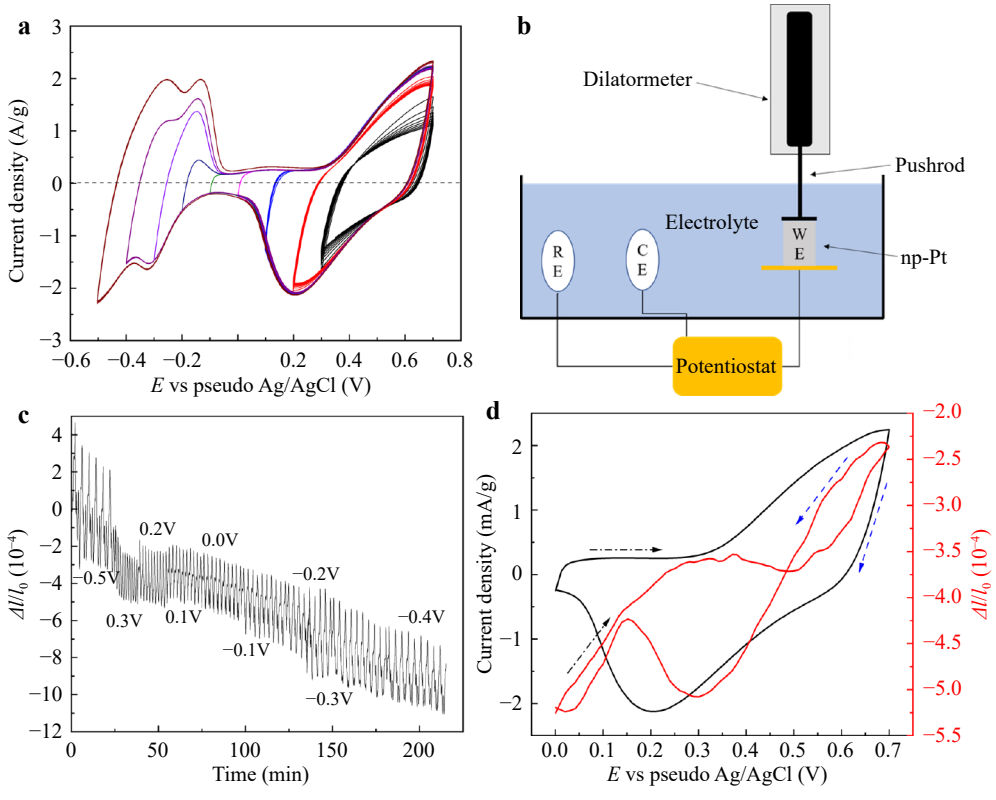


**Figure 4** Actuation performance of np-Pt in 1 mol $L^{-1}$ $H_2SO_4$. (a) Cyclic voltammogram for np-Pt in different potential windows. The upper vertex potential was fixed at 0.7 V. The lower vertex potential was initially −0.5 V and then decreased by 0.1 V after each 10 scans from 0.3 V. The scan rate is 10 mV/s. (b) Schematic of the in-situ dilatometry setup. (c) Cyclic length change during potential sweep; RE: reference electrode, CE: counter electrode, WE: working electrode. (d) Cyclic relative length change and current density during potential sweep from 0 to 0.7 V, with data taken from (c).

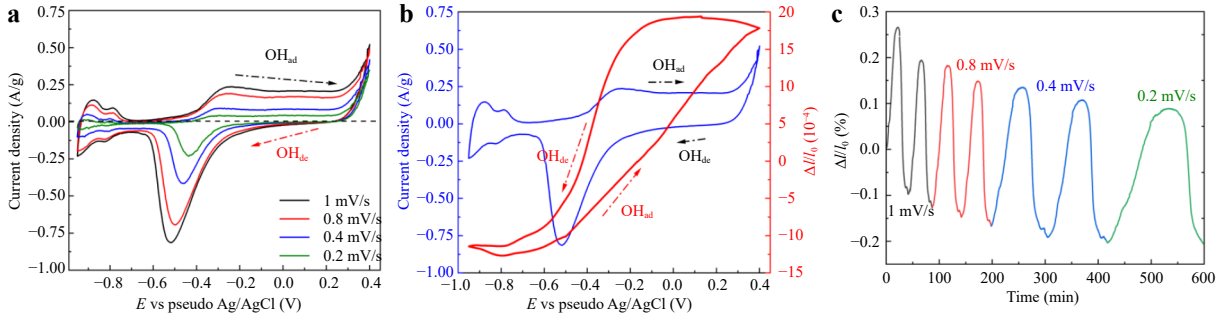


**Figure 5** Actuation performance of np-Pt in 1 mol $L^{-1}$ KOH. (a) Cyclic voltammogram of the np-Pt 1 mol $L^{-1}$ KOH at different scan rates. (b) Current density and relative length change $\Delta l/l_0$ as a function of electrode potential. (c) Cyclic strain variation during potential sweep at different scan rates.

and $Y_{eff}$ is the effective macroscopic Young's modulus. The surface stress-induced macroscopic strain is supposed to be isotropic within the nanoporous samples. Thus, $\rho$ = 8.58 g/cm³ and $\varepsilon_{max} = \Delta V/V_0 \approx 3\Delta l/l_0$ = 1.11% for np-Pt[28]. $Y_{eff}$ is estimated to be 26.9 GPa according to the Gibbs–Ashby equation ($Y_{eff}/Y_0 = \varphi^2$)[39], with $Y_0$ representing the Young's modulus of massive Pt (168 GPa) and $\varphi$ representing the solid volume fraction of np-Pt (0.40). The energy density parameters $W_V$ and $W_M$ were determined to be 1.64 MJ/m³ and 191 J/kg, respectively. Remarkably, the $W_V$ and $W_M$ of the ultrafine np-Pt are substantially improved compared to the np-Pt synthesized by consolidating commercial Pt black with a nanocrystal size of 6 nm[11, 40]. The work density of the proposed np-Pt actuator is over 40 times greater than that of skeletal muscle (approximately 40 kJ/m³[41]). Even in comparison to representative high stiffness and work density piezoceramics, the proposed np-Pt in this work is distinguished by its approximately 100 times lower operating voltage (np-Pt: approximately 1.0 V; piezoceramics: in the order of 100 V) and more than two times larger strain amplitude (np-Pt: 0.4%; piezoceramics: 0.1%–0.2%).

## 4 Conclusions

Mechanically robust np-Pt bulk samples with a ligament size down to 2 nm were fabricated in this study for the first time using electrochemical dealloying approaches. Such a small ligament size has never been achieved in crack-free monolithic nanoporous metallic samples in the literature. The novel np-Pt material exhibits a large electrochemically active surface area even at 15% compressive strain and good thermal stability. In-situ dilatometry experiments reveal the excellent actuation performances of the ultrafine np-Pt: an operating voltage down to 1.0 V, a linear strain amplitude up to 0.37%, and a work density of 1.64 $MJ/m^3$. The exemplary application of np-Pt in actuators confirmed the remarkable potential of the proposed ultrafine np-Pt bulk materials in a variety of surface- or interface-controlled applications such as electrochemical catalysts, actuators, and strain sensors. The large surface-to-volume ratio and macroscopic body of the np-Pt bulk materials developed in this study can also contribute to the field of nanomechanics by serving as a model material for revealing size effects in nanoporous metals with structure sizes smaller than 10 nm.

## Acknowledgments

We thank Prof. Jiuhui Han from Tianjin University of Technology for his assistance with TEM measurements.

## Declaration of conflicting interests

The authors declare no conflicting interests regarding the content of this article.

## References

[1] Germain, J., Hradil, J., Fréchet, J. M. J., Svec, F. (2006). High surface area nanoporous polymers for reversible hydrogen storage. *Chem. Mater.* 18, 4430–4435.

[2] Jiang, H. L., Liu, B., Lan, Y. Q., Kuratani, K., Akita, T., Shioyama, H., Zong, F. Q., Xu, Q. (2011). From metal–organic framework to nanoporous carbon: toward a very high surface area and hydrogen uptake. *J. Am. Chem. Soc.* 133, 11854–11857.

[3] Rouya, E., Cattarin, S., Reed, M. L., Kelly, R. G., Zangari, G. (2012). Electrochemical characterization of the surface area of nanoporous gold films. *J. Electrochem. Soc.* 159, K97–K102.

[4] Zhang, J. T., Li, C. M. (2012). Nanoporous metals: fabrication strategies and advanced electrochemical applications in catalysis, sensing and energy systems. *Chem. Soc. Rev.* 41, 7016–7031.

[5] Bansal, V., Jani, H., Du Plessis, J., Coloe, P. J., Bhargava, S. K. (2008). Galvanic replacement reaction on metal films: a one‐step approach to create nanoporous surfaces for catalysis. *Adv. Mater.* 20, 717–723.

[6] Lu, G. M., Zhao, X. S. (2004). Nanoporous Materials: Science and Engineering. London: Imperial College Press.

[7] Yuan, H. C., Yost, V. E., Page, M. R., Stradins, P., Meier, D. L., Branz, H. M. (2009). Efficient black silicon solar cell with a density-graded nanoporous surface: optical properties, performance limitations, and design rules. *Appl. Phys. Lett.* 95, 123501.

[8] Gan, L., Heggen, M., O'Malley, R., Theobald, B., Strasser, P. (2013). Understanding and controlling nanoporosity formation for improving the stability of bimetallic fuel cell catalysts. *Nano Lett.* 13, 1131–1138.

[9] Gan, L., Cui, C. H., Rudi, S., Strasser, P. (2014). Core–shell and nanoporous particle architectures and their effect on the activity and stability of Pt ORR electrocatalysts. *Top. Catal.* 57, 236–244.

[10] Jin, H. J., Weissmüller, J. (2010). Bulk nanoporous metal for actuation. *Adv. Eng. Mater.* 12, 714–723.

[11] Weissmüller, J., Viswanath, R. N., Kramer, D., Zimmer, P., Würschum, R., Gleiter, H. (2003). Charge-induced reversible strain in a metal. *Science* 300, 312–315.

[12] King, T. G., Preston, M. E., Murphy, B. J. M., Cannell, D. S. (1990). Piezoelectric ceramic actuators: a review of machinery applications. *Precis. Eng.* 12, 131–136.

[13] Newcomb, C. V., Flinn, I. (1982). Improving the linearity of piezoelectric ceramic actuators. *Electron. Lett.* 18, 442–444.

[14] Lendlein, A., Gould, O. E. C. (2019). Reprogrammable recovery and actuation behaviour of shape-memory polymers. *Nat. Rev. Mater.* 4, 116–133.

[15] Hu, L., Zhang, Q., Li, X., Serpe, M. J. (2019). Stimuli-responsive polymers for sensing and actuation. *Mater. Horiz.* 6, 1774–1793.

[16] Sun, H. N., Wang, X. J., Sun, Q. Z., Zhang, X. X., Ma, Z., Guo, M. Y., Sun, B. W., Zhu, X. P., Liu, Q. D., Lou, X. J. (2020). Large energy storage density in $BiFeO_3$-$BaTiO_3$-$AgNbO_3$ lead-free relaxor ceramics. *J. Eur. Ceram. Soc.* 40, 2929–2935.

[17] Choi, S. B., Han, Y. M. (2016). Piezoelectric Actuators: Control Applications of Smart Materials. USA: CRC Press.

[18] Pelrine, R., Kornbluh, R., Pei, Q. B., Joseph, J. (2000). High-speed electrically actuated elastomers with strain greater than 100%. *Science* 287, 836–839.

[19] Haiss, W. (2001). Surface stress of clean and adsorbate-covered solids. *Rep. Prog. Phys.* 64, 591–648.

[20] Shi, S., Li, Y., Ngo-Dinh, B. N., Markmann, J., Weissmüller, J. (2021). Scaling behavior of stiffness and strength of hierarchical network nanomaterials. *Science* 371, 1026–1033.

[21] Weissmüller, J., Cahn, J. W. (1997). Mean stresses in microstructures due to interface stresses: a generaliza-

tion of a capillary equation for solids. *Acta Mater.* 45, 1899–1906.

[22] Viswanath, R. N., Kramer, D., Weissmüller, J. (2008). Adsorbate effects on the surface stress–charge response of platinum electrodes. *Electrochim. Acta.* 53, 2757–2767.

[23] Shi, S., Markmann, J., Weissmüller, J. (2017). Actuation by hydrogen electrosorption in hierarchical nanoporous palladium. *Philos. Mag.* 97, 1571–1587.

[24] Hakamada, M., Nakano, H., Furukawa, T., Takahashi, M., Mabuchi, M. (2010). Hydrogen storage properties of nanoporous palladium fabricated by dealloying. *J. Phys. Chem. C.* 114, 868–873.

[25] Biener, J., Wittstock, A., Zepeda-Ruiz, L. A., Biener, M. M., Zielasek, V., Kramer, D., Viswanath, R. N., Weissmüller, J., Bäumer, M., Hamza, A. V. (2009). Surface-chemistry-driven actuation in nanoporous gold. *Nat. Mater.* 8, 47–51.

[26] Jin, H. J., Parida, S., Kramer, D., Weissmüller, J. (2008). Sign-inverted surface stress-charge response in nanoporous gold. *Surf. Sci.* 602, 3588–3594.

[27] Mathur, A., Erlebacher, J. (2007). Size dependence of effective Young's modulus of nanoporous gold. *Appl. Phys. Lett.* 90, 061910.

[28] Jin, H. J., Wang, X. L., Parida, S., Wang, K., Seo, M., Weissmüller, J. (2010). Nanoporous Au− Pt alloys as large strain electrochemical actuators. *Nano Lett.* 10, 187–194.

[29] Erlebacher, J., Aziz, M. J., Karma, A., Dimitrov, N., Sieradzki, K. (2001). Evolution of nanoporosity in dealloying. *Nature* 410, 450–453.

[30] Mani, P., Srivastava, R., Strasser, P. (2011). Dealloyed binary $PtM_3$ (M= Cu, Co, Ni) and ternary $PtNi_3M$ (M= Cu, Co, Fe, Cr) electrocatalysts for the oxygen reduction reaction: performance in polymer electrolyte membrane fuel cells. *J. Power Sources* 196, 666–673.

[31] McCue, I., Benn, E., Gaskey, B., Erlebacher, J. (2016). Dealloying and dealloyed materials. *Annu. Rev. Mater. Res.* 46, 263–286.

[32] Binninger, T., Fabbri, E., Kötz, R., Schmidt, T. J. (2014). Determination of the electrochemically active surface area of metal-oxide supported platinum catalyst. *J. Electrochem. Soc.* 161, H121–H128.

[33] Watt-Smith, M. J., Friedrich, J. M., Rigby, S. P., Ralph, T. R., Walsh, F. C. (2008). Determination of the electrochemically active surface area of Pt/C PEM fuel cell electrodes using different adsorbates. *J. Phys. D: Appl. Phys.* 41, 174004.

[34] Gasteiger, H. A., Kocha, S. S., Sompalli, B., Wagner, F. T. (2005). Activity benchmarks and requirements for Pt, Pt-alloy, and non-Pt oxygen reduction catalysts for PEMFCs. *Appl. Catal. B: Environ.* 56, 9–35.

[35] Fujigaya, T., Okamoto, M., Nakashima, N. (2009). Design of an assembly of pyridine-containing polybenzimidazole, carbon nanotubes and Pt nanoparticles for a fuel cell electrocatalyst with a high electrochemically active surface area. *Carbon* 47, 3227–3232.

[36] Seo, M., Makino, T., Sato, N. (1986). Piezoelectric response to surface stress change of platinum electrode. *J. Electrochem. Soc.* 133, 1138–1142.

[37] Jia, Y. Y., Su, J. Y., Chen, Z. B., Tan, K., Chen, Q. L., Cao, Z. M., Jiang, Y. Q., Xie, Z. X., Zheng, L. S. (2015). Composition-tunable synthesis of Pt–Cu octahedral alloy nanocrystals from PtCu to $PtCu_3$ *via* underpotential-deposition-like process and their electro-catalytic properties. *RSC Adv.* 5, 18153–18158.

[38] Uchino, K. (1996). Piezoelectric Actuators and Ultrasonic Motors. New York: Springer.

[39] Gibson, L. J. (2003). Cellular solids. *MRS Bull.* 28, 270–274.

[40] Lüth, H. (1995). Surfaces and Interfaces of Solid Materials. 3rd ed. Berlin: Springer.

[41] Madden, J. D. W., Vandesteeg, N. A., Anquetil, P. A., Madden, P. G. A., Takshi, A., Pytel, R. Z., Lafontaine, S. R., Wieringa, P. A., Hunter, I. W. (2004). Artificial muscle technology: physical principles and naval prospects. *IEEE J. Oceanic Eng.* 29, 706–728.